ARTICLE OPEN

Check for updates

Stress corrosion cracking of X80 steel heat-affected zone in a near-neutral pH solution containing *Bacillus cereus*

Bo Liu[1,2], Jike Yang[1], Cuiwei Du[1,3,4 ✉], Zhiyong Liu [1,3,4 ✉], Wei Wu[1] and Xiaogang Li[1,3,4]

Bacillus cereus (*B. cereus*) is observed to have varying effects on the stress corrosion cracking (SCC) sensitivity of different microstructures in the simulated heat-affected zone (HAZ) of X80 steel. At open circuit potential (OCP), the SCC sensitivity of different microstructures increased from 3.40–7.49% in an abiotic medium to 10.22–15.17% in a biotic medium. At -0.9 V (SCE), it increased from 22.81–26.51% to 35.76–39.60%. The increment in SCC sensitivity upon exposure to *B. cereus* was highest in the coarse-grained HAZ (7.68 and 16.79% at OCP and -0.9 V, respectively), followed by the intercritical and fine-grained HAZs. Owing to differences in the phase composition, grain boundary type, dislocation density, and surface volta potential, the initial adhesion number and position of *B. cereus* in the microstructure of the HAZ were differed, resulting in different sensitivities to SCC.

INTRODUCTION

The X80 pipeline steel is widely accepted as one of the most economical seamless and welded pipeline steels owing to its high resistance, strength, and weldability. Although corrosion accidents are minimized in pipes, which are manufactured and operated in compliance with regulations, they are not completely eliminated owing to the special microstructure of welded joints[1–3]. The change in the local microstructure during the welding thermal cycle is attributed to the corrosion behavior of the corresponding weld region[4–6]. The heat-affected zone (HAZ) deserves special attention for its role in corrosion resistance as the physical, mechanical, and chemical properties of the alloy therein differ from those observed in the parent metal area. In conventional steels, the HAZ can be broken down into three crucial components: the intercritical HAZ (ICHAZ), fine-grained HAZ (FGHAZ), and coarse-grained HAZ (CGHAZ), with each component exhibiting a distinct microstructure.

Over the past several decades, a significant number of studies on the corrosion of welded joints have focused on galvanic, stress, and fatigue corrosions in ocean atmosphere, soil solution, and other environments[7–9]. Recently, microbiologically influenced corrosion (MIC) of welded joints has attracted the attention of researchers[10–12]. Arun et al.[13] investigated the microstructural changes in stainless steel, including the formation of secondary and intergranular austenite in weld seams that reduced the levels of alloying elements and resulted in MIC. Antony et al.[14] reported sulfate-reducing bacteria (SRB) attack to occur preferentially in the ferrite phase of a 2205 duplex stainless steel weldment, while being restricted to the austenite phase of the parent metal. Liduino et al.[15] conducted a comparative study on the welding area of X65 steel and observed the welding region to be more prone to biofilm development, which is primarily related to the surface roughness. Evidently, the microstructure of stainless or carbon steel substantially affects the corrosion sensitivity and its underlying mechanisms.

Most equipments are subjected to stress during service. Subsequently, the relationship between microorganisms and stress corrosion is being studied[16–18]. SRB enhances the brittle fracture characteristics of carbon steel by facilitating hydrogen recombination and the diffusion of atomic hydrogen into the metal[19]. SRB has different control mechanisms for stress corrosion cracking (SCC) of 980 steel at different culture times by hydrogen permeation, which is also closely related to that under a cathodic potential[20]. Under a cathodic potential, SRB-assisted pitting and promotion of hydrogen permeation into steel facilitate crack initiation and propagation, responsible for the increase in SCC susceptibility[21]. Many studies have focused on SRB, but little has been reported on *Bacillus cereus* (*B. cereus*), a typical nitrate-reducing bacteria (NRB) that is widespread in soils and oceans[22–24]. The only study on stress corrosion by NRB reports that the ammonia produced by its metabolism leads to dezincification and the subsequent fracture of the copper alloy[25]. Previous studies have confirmed that X80 steel exhibits high corrosion rates and SCC susceptibility in a *Bacillus cereus* (*B. cereus*) environment[26,27]. The effect of *B. cereus* on the deterioration of weld HAZ is scarcely explored. Thus, there is a research gap in the investigation of stress corrosion of X80 steel in the HAZ upon exposure to *B. cereus* in a near-neutral pH environment.

In this study, different HAZ microstructures were obtained via heat treatment to simulate the weld HAZ. The effects of *B. cereus* on the electrochemical properties, surface morphology, and composition of the HAZ were determined. The SCC sensitivity of the HAZ to the *B. cereus* system under open circuit and cathodic potentials has been discussed. Furthermore, the initial adhesion number and position of *B. cereus* in the HAZ and their relationship with stress have been discussed.

RESULTS AND DISCUSSION

Microstructure characterization of HAZ

The morphologies of the real and simulated HAZ microstructures were compared, as shown in Fig. 1a–c. The morphologies of the simulated HAZ are observed to be similar to those of the real HAZ. ICHAZ is mainly composed of granular bainite with the grain size

[1]Institute for Advanced Materials and Technology, University of Science and Technology Beijing, Beijing 100083, China. [2]School of Materials Science and Engineering, Xi'an Shiyou University, Xi'an 710065, China. [3]National Materials Corrosion and Protection Scientific Data Center, Beijing 100083, China. [4]Beijing Advanced Innovation Center for Materials Genome Engineering, University of Science and Technology Beijing, Beijing 100083, China. ✉email: dcw@ustb.edu.cn; liuzhiyong7804@126.com

ranging from 2–10 μm. Upon increasing the heating temperature, FGHAZ is bainite and quasi-polygonal ferrite with the grain size ranging 10–15 μm. Upon further heating, the grain size increases to 15–30 μm, and CGHAZ is dominated by granular bainite with a prior austenite grain boundary. The higher heating temperature makes atom diffusion easier, reduces the grain boundary migration resistance, and increases the grain size to form a proto-austenite grain boundary.

The Vickers microhardness from the HAZ to base metal was measured and compared with that of the corresponding simulated HAZ (Fig. 2). The Vickers microhardness test with a load of 100 g was repeated at least three times in different areas
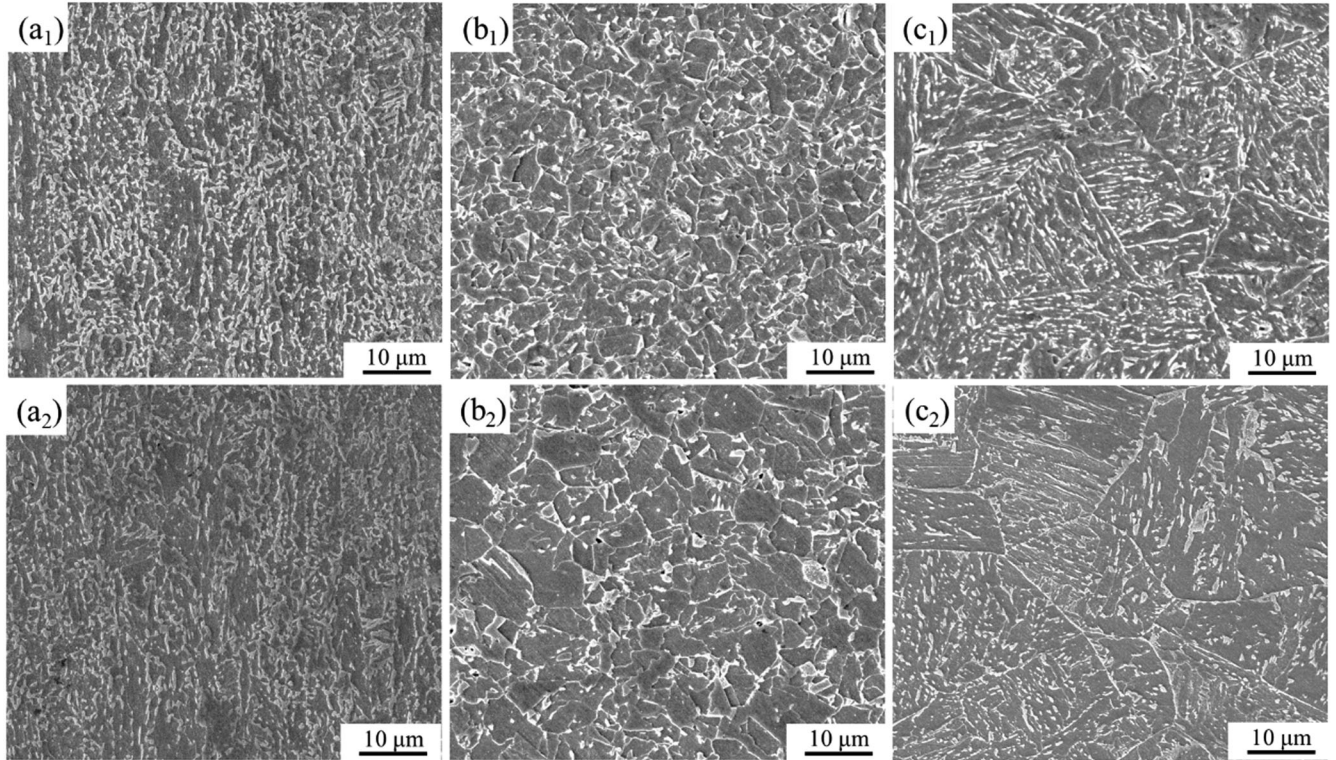

Fig. 1 SEM morphology comparison of simulated HAZ microstructures and corresponding real ones. a_1–c_1 show real ICHAZ, FGHAZ, and CGHAZ. a_2–c_2 show simulated ICHAZ, FGHAZ, and CGHAZ.
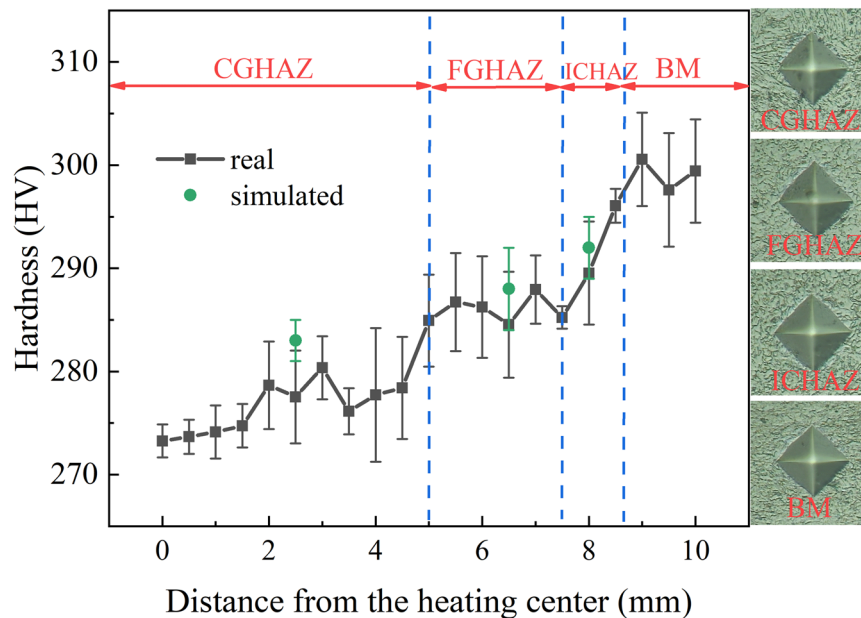

Fig. 2 Microhardness of HAZ microstructures. The change value between the Vickers hardness of the real HAZ and the distance from the heating center, as well as the Vickers hardness values of the simulated HAZ after different heat treatments (error bars stand for the standard deviations from three independent samples).
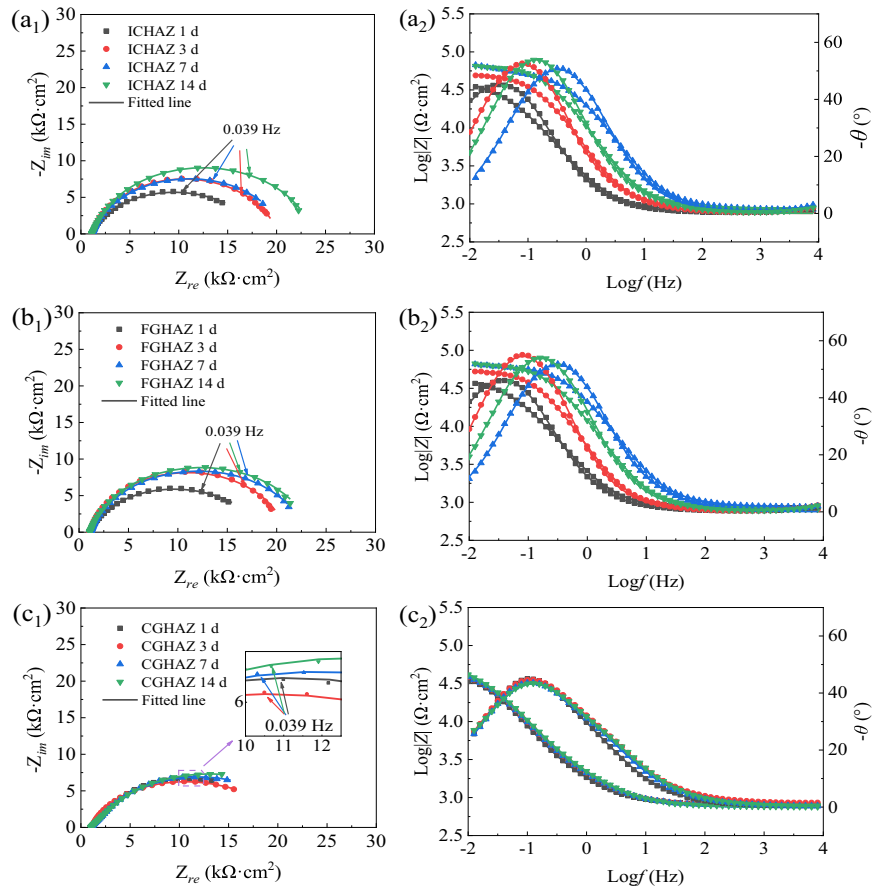
Fig. 3 EIS results of HAZ immersed in abiotic medium for different durations. a_1, a_2 show ICHAZ. b_1, b_2 show FGHAZ. c_1, c_2 show CGHAZ.
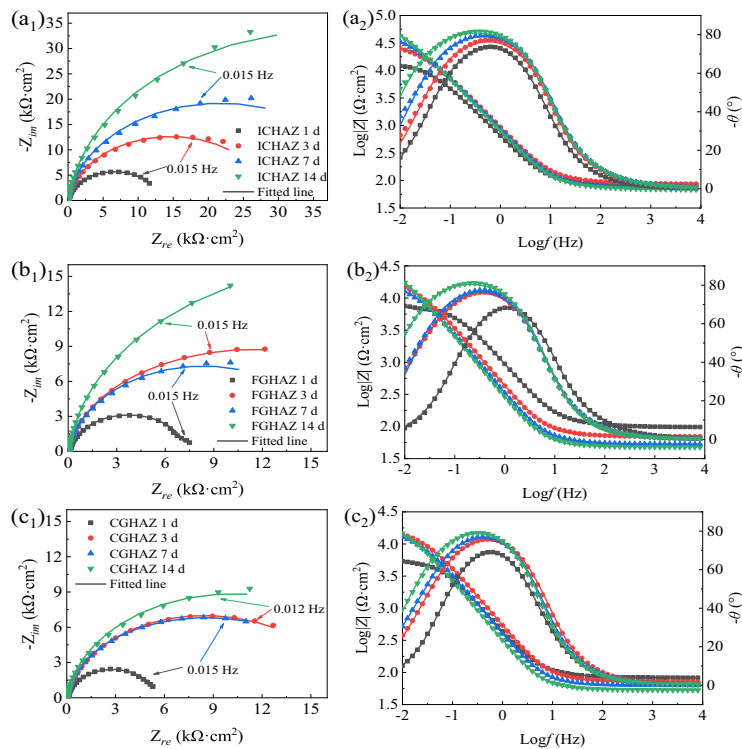
Fig. 4 EIS results of HAZ immersed in biotic medium for different durations. a_1, a_2 show ICHAZ. b_1, b_2 show FGHAZ. c_1, c_2 show CGHAZ.

for each HAZ microstructure. The results showed that the hardness of the simulated HAZ microstructures was similar to that of the real HAZ but slightly lower than that of the parent metal. Previous studies have reported air cooling to refine the crystal grains of steel and significantly improve its mechanical properties[28]. The morphology and hardness of the simulated HAZ were similar to those of the real HAZ. Therefore, the simulated microstructure prepared using this method was concluded to effectively map a typical HAZ microstructure.

Electrochemical characterization

The EIS results of different HAZ microstructures in abiotic and biotic media with their immersion times are compared in Figs. 3 and 4. In the abiotic medium, the three different microstructures exhibited relatively complete capacitive and reactance arcs with increasing immersion time. The changes in the radii and capacitance arcs corresponding to different immersion times and microstructures were small, indicating a slight effect of the corrosion rate on the immersion time in an anaerobic environment. In the biotic medium, the arc radius of the reactance of different microstructures increased with increasing immersion time, indicating a gradual decrease of the corrosion rate. The phase angle showed one time constant, indicating only one polarization potential to affect the electrode reaction in the system. Moreover, the bacteria and biofilm did not increase the electrode reaction[22].

The EIS results were used to further analyze the impedance values by fitting the data with an equivalent circuit model, as

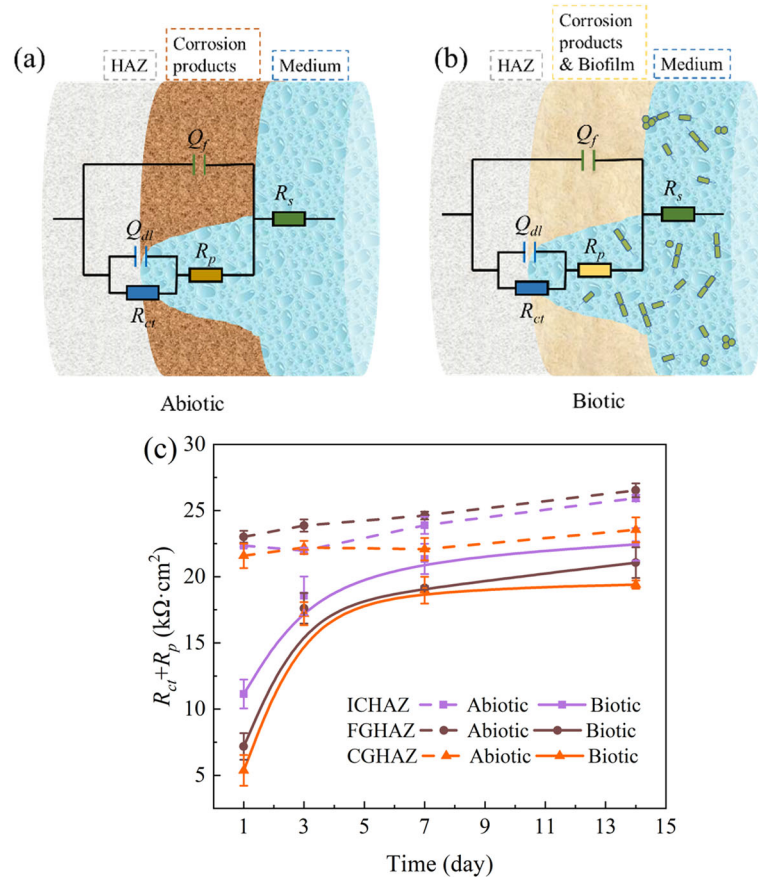**Fig. 5 Electrical equivalent circuit used for fitting the EIS spectra. a** is abiotic, **b** is biotic and **c** is $R_{ct} + R_p$ value (error bars stand for the standard deviations from three independent samples).
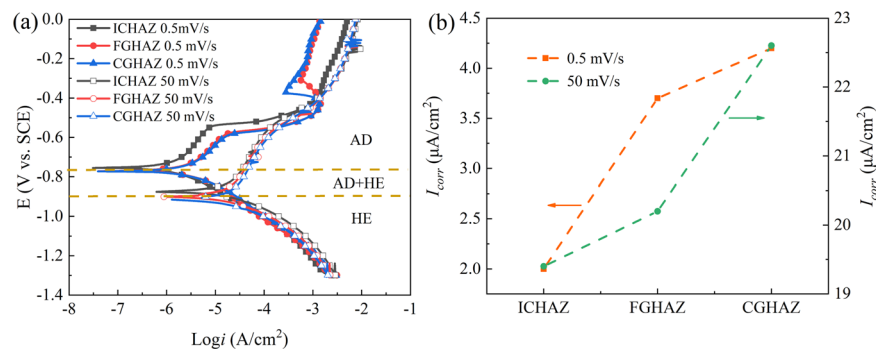

Fig. 6 Polarization curves of the HAZ measured at fast (50 mV s^{-1}) and slow (0.5 mV s^{-1}) potential scanning rates in biotic medium after 3 d. a is polarization curve. **b** is Tafel fitting corrosion current density.
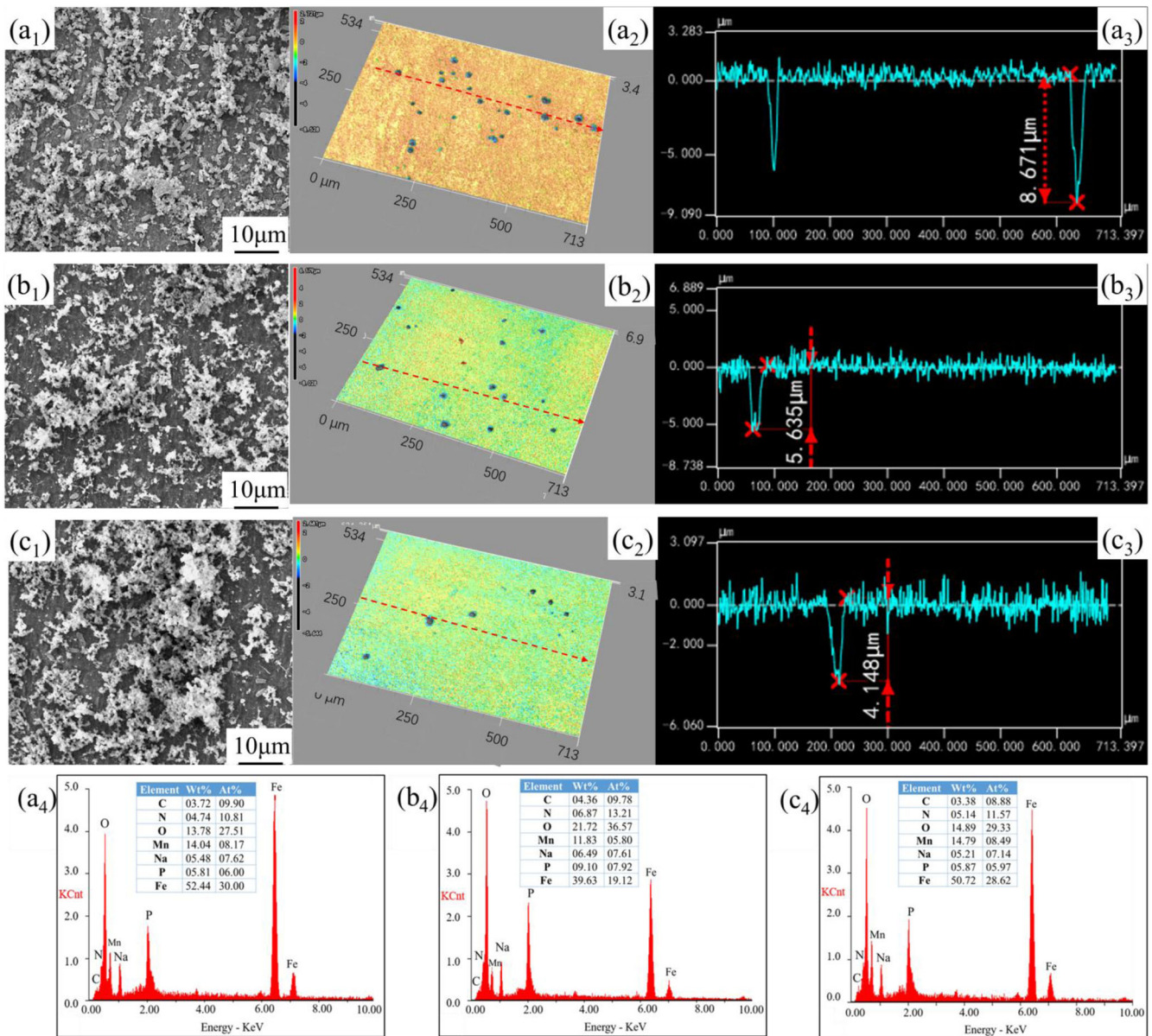
Fig. 7 Surface morphology and topography after rust removal and product composition of HAZ immersed in biotic medium for 14 d.
a_1–a_4 show ICHAZ. b_1–b_4 show FGHAZ. c_1–c_4 show CGHAZ.

shown in Fig. 5a, b. The obtained fitting electrochemical parameters are summarized in Supplementary Tables 1 and 2. In the circuit, R_s is the solution resistance, Q_f is the capacitance of the corrosion products in the abiotic medium and that of the mixed layer of corrosion product and biofilm in the biotic medium, R_p is the pore resistance in abiotic or biotic medium, and Q_{dl} and R_{ct} represent the double layer capacitance and charge transfer resistance, respectively. It is known that the value of $R_{ct} + R_p$ reflects the corrosion rate, with a higher value indicating a lower corrosion rate.

Figure 5c depicts the $R_{ct} + R_p$ variation of the fitting results. For the three different microstructures, the $R_{ct} + R_p$ values in the abiotic medium increase slightly with immersion time, but the overall change is small. In the biotic medium, the $R_{ct} + R_p$ values show an increasing trend over time, but the values are lower than the corresponding values in the abiotic medium. Based on these EIS results, the following three conclusions were drawn. First, the corrosion rates of different microstructures in the biotic medium were higher than their counterparts in the abiotic medium for the

same immersion time. Second, the $R_{ct} + R_p$ value of CGHAZ was the lowest of the three different microstructures for the same immersion time, regardless of the type of medium (biotic or abiotic), indicating that CGHAZ had the weakest ability to hinder charge transfer and the highest corrosion rate. Third, compared with the abiotic medium, the effect of the MIC on the different microstructures was particularly evident during the period of 1–3 d.

Figure 6 shows the sweep potential polarization curves of different HAZ microstructures and the corresponding Tafel fitting results. The different microstructures are observed to have slight effect on the potentiodynamic polarization results. When the scanning rate is 0.5 mV s^{-1}, the electrochemical reaction of carbon steel is in a quasi-equilibrium state. When the potential scanning rate is adequately high (~50 mV s^{-1}), the electrochemical reaction reaches another quasi-equilibrium state. The polarization curves measured at slow and fast scanning rates of 0.5 and 50 mV s^{-1}, respectively, divide the null-current position into three zones: AD-dominated, HE-dominated, and both AD and HE co-existing
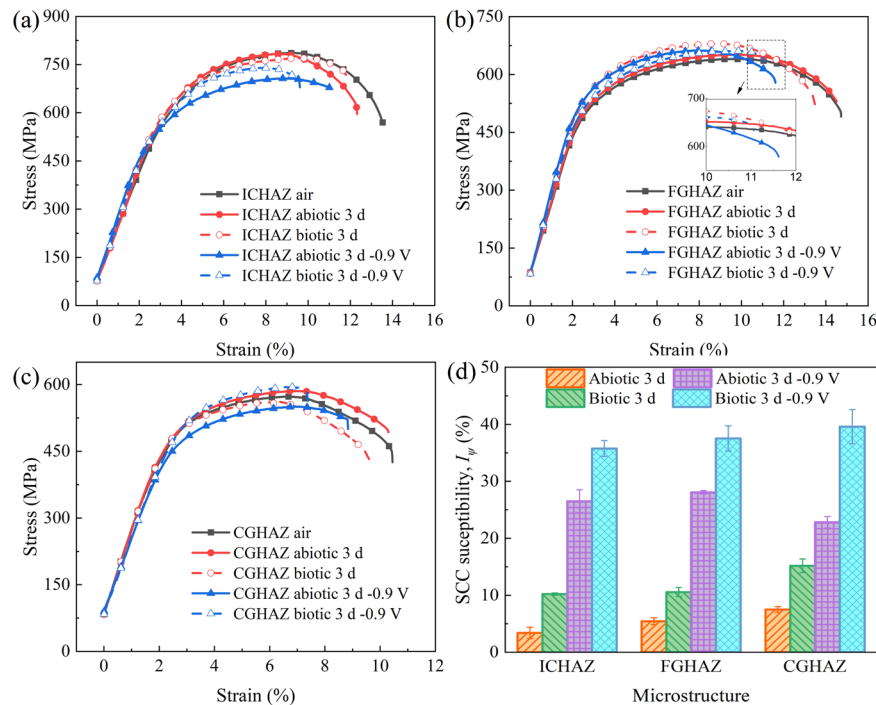
Fig. 8 Stress-strain curves of HAZ in different test environments. a is ICHAZ. **b** is FGHAZ. **c** is CGHAZ and **d** is SCC susceptibility (error bars stand for the standard deviations from three independent samples).

zones[29,30]. Figure 6a shows that −0.9 V is the initial potential of hydrogen embrittlement, but this does not indicate any effect of hydrogen on the fracture.

To further quantify the potentiodynamic polarization curves, the Tafel extrapolation method was used to evaluate the corrosion current density (I_{corr}). The results showed that the current densities of the different microstructures followed the order: $I_{CGHAZ} > I_{FGHAZ} > I_{ICHAZ}$, regardless of the scanning rate. The different current densities were related both to the structure of the material and the effect of bacteria on its surface. It is noteworthy that an inflection point occurred when the anode potential was −0.3 V, which is the oxidation potential of ferrous materials such as $FeCO_3$ to Fe_2O_3 and Fe_3O_4[26].

Surface morphology and composition analysis
The surface and corrosion morphologies of the different HAZ microstructures after 14 d of immersion in a biotic medium are shown in Fig. 7. Both biofilm and corrosion products are observed to cover the surface of the sample. The biofilm clusters are composed of rod-shaped bacteria with a length of 2–3 μm. Based on the monitoring of bacterial growth in a previous work and observation of morphology, it was determined that *B. cereus* can survive for at least 14 d in a pre-given carbon source and oxygen-free environment[26]. No evident differences were observed in the surface morphologies of the three microstructures; however, upon removal of the corrosion products, the corrosion morphology of CGHAZ was severe, while that of ICHAZ was slight. These results conformed with those of the electrochemical test, which indicated that the bacteria had the most prominent corrosion effect on CGHAZ during the two-week period. The EDX results show that the surface products are mainly composed of Fe, O, and P, and contain small amounts of Mn and Na, wherein P and O are the main components of the cells and Na and Mn are primarily contained in the medium and materials, respectively.

SSRT results
Figure 8 shows the SSRT test results and SCC susceptibility of the different HAZ microstructures at OCP and −0.9 V in air and abiotic and biotic media for 3 d. Following the heat treatment, compared with the yield strength of the parent metal, those of ICHAZ, FGHAZ, and CGHAZ reduce to 776, 671, and 582 MPa, respectively, in air. The elongation of ICHAZ and FGHAZ increase slightly, while that of CGHAZ decreases slightly. Under the OCP and cathodic potential in the abiotic and biotic media, the SCC susceptibility index and reduction in area I_ψ were calculated using Eq. 1 and are plotted in Fig. 8d. It is observed that the I_ψ value of the HAZ in the biotic medium is greater than that in the abiotic medium, and this applies for −0.9 V. The differences in I_ψ for the biotic and abiotic media at OCP and −0.9 V were compared, and the corresponding results showed that ICHAZ, FGHAZ, and CGHAZ were 6.67%, 5.11%, and 6.81%, respectively, at the OCP, and 14.25%, 8.47%, and 17.79%, respectively, at −0.9 V. Compared with the I_ψ values of ICHAZ and FGHAZ, that of the CGHAZ was the largest, indicating that the bacterial system had the most significant susceptibility to SCC. Furthermore, it was found that the cathodic potential increased the SCC sensitivity of the bacterial system to each microstructure.

Figure 9 shows the fracture morphology of the different HAZ microstructures at OCP and −0.9 V in abiotic and biotic media. At OCP, all the fractures exhibit a slight shrinkage phenomenon. When observing the break initiation, the ICHAZ and FGHAZ show small dimples in both the abiotic and biotic media, indicating the presence of ductile fracture characteristics. However, the fluvial morphology of CGHAZ indicates that the fracture is brittle. At −0.9 V, the dimples of both ICHAZ and FGHAZ are deep and small in both the abiotic and biotic media. The dimples of the CGHAZ microstructure are small (in number) and shallow, and the typical tearing edge characteristics indicate that the CGHAZ microstructure has high brittleness. For the different microstructures, the −0.9 V potential is the initial potential for hydrogen embrittlement, but the CGHAZ fracture shows the characteristics of a brittle fracture at this potential, indicating that the environment of *B. cereus* promotes hydrogen embrittlement.
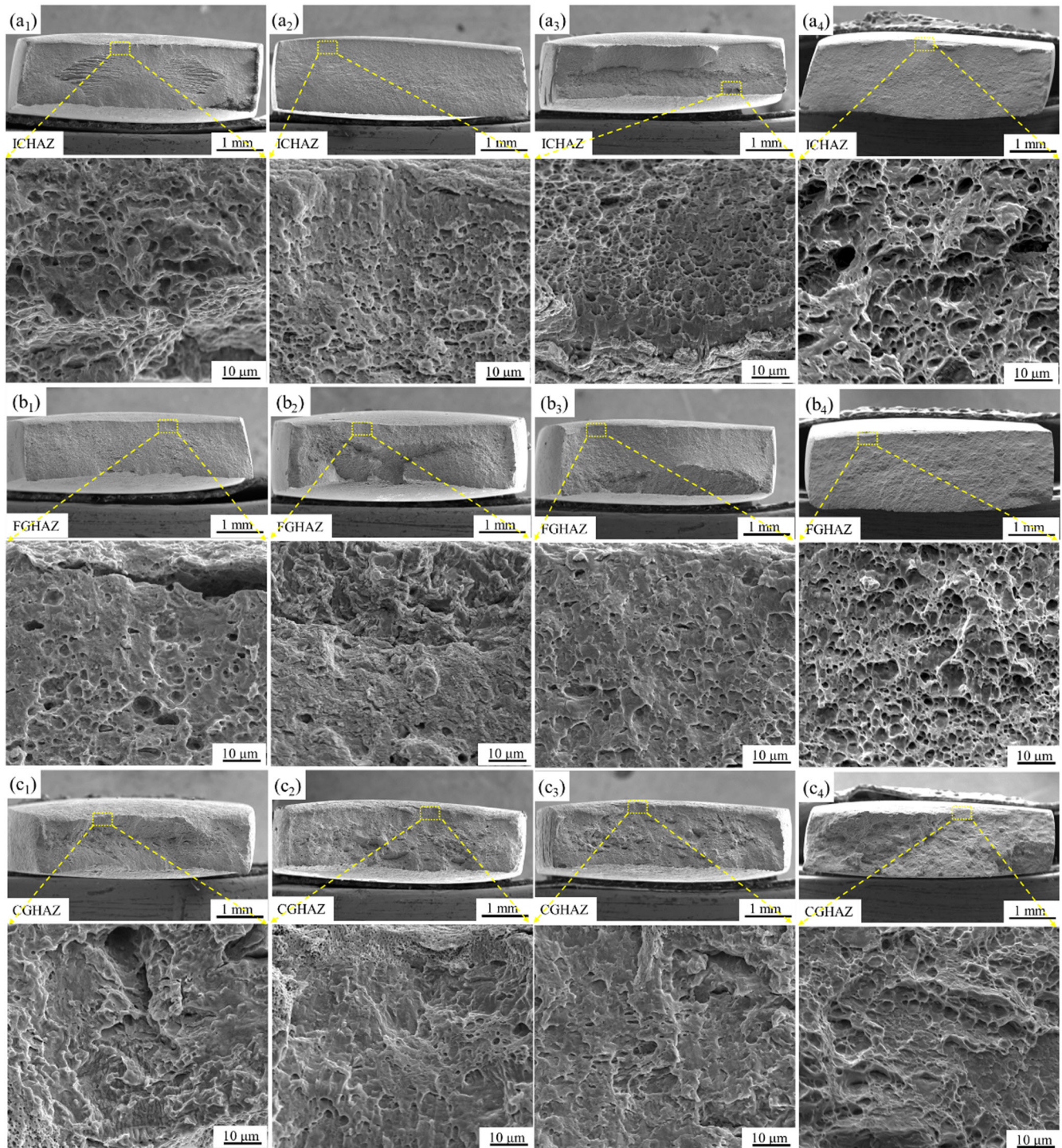
Fig. 9 Fracture morphologies of HAZ after cathodic polarization at −0.9 V for 3 d in biotic medium. a is ICHAZ. **b** is FGHAZ. **c** is CGHAZ. Subscripts 1–4 are abiotic, biotic, abiotic @−0.9 V and biotic @−0.9 V, respectively.

The lateral morphologies of the above fractures were examined in detail, and the corresponding results are shown in Fig. 10. At the OCP, the surfaces of the samples exhibit a corrosion morphology, and the subsequent characteristics are more evident in the presence of the bacteria. In the secondary crack morphology, the crack size of CGHAZ is observed to be larger than that of the other microstructures. At −0.9 V, no evident corrosion phenomenon is observed on the surface of the samples in both abiotic and biotic media, indicating that this potential effectively inhibited the corrosion reaction. The secondary crack

size is larger in the bacterial system than that in the sterile medium, indicating that CGHAZ is more sensitive to SCC in the bacterial system.

Effect of different HAZ microstructures on bacteria initial adhesion
Based on the EIS results, potentiodynamic polarization curves, and surface morphology, it was determined that the bacteria had the greatest effect on the corrosion of CGHAZ. Previous studies have
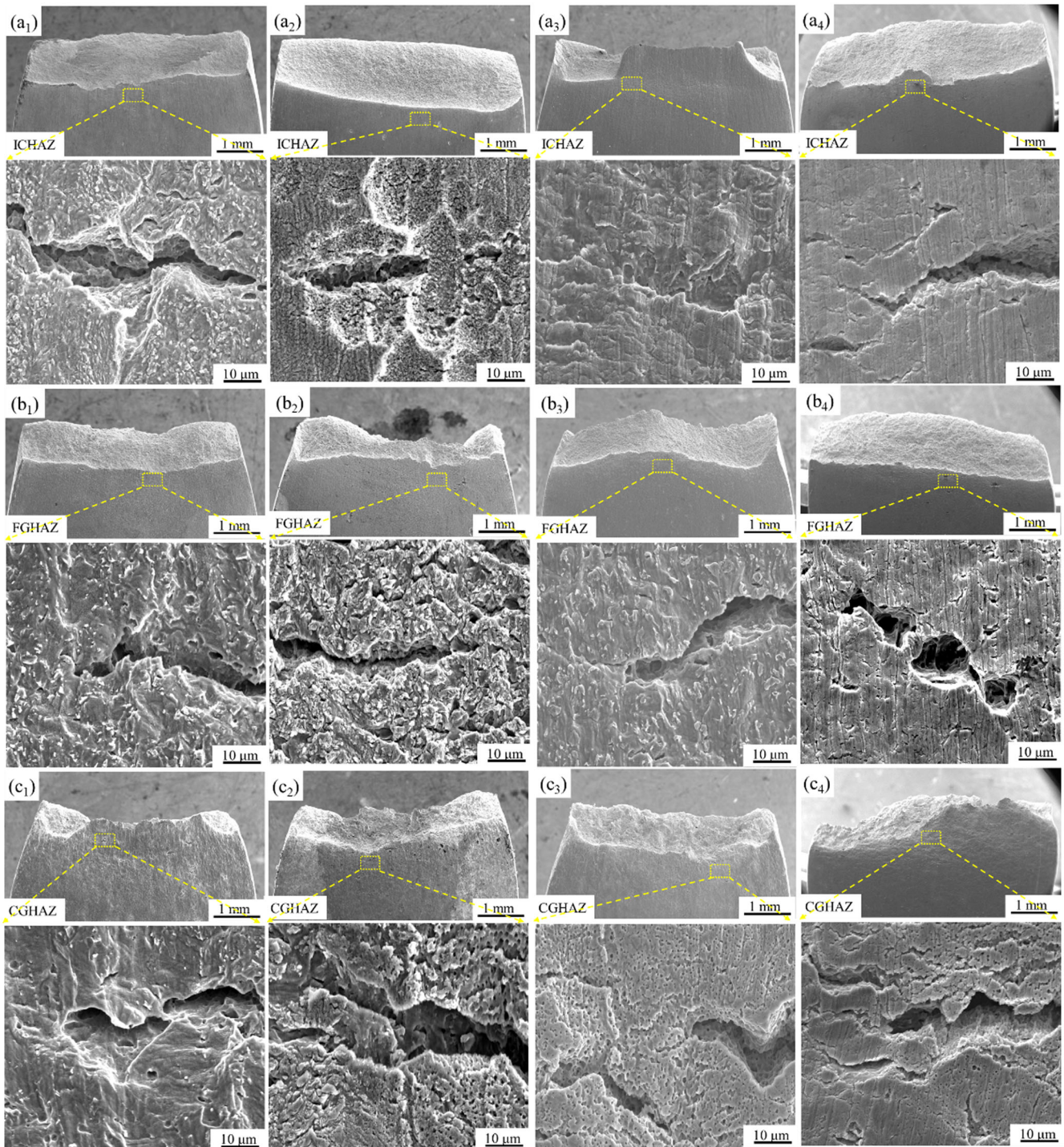
Fig. 10 Lateral morphologies of HAZ after cathodic polarization at −0.9 V for 3 d in biotic medium. a is ICHAZ. **b** is FGHAZ. **c** is CGHAZ. Subscripts 1–4 are abiotic, biotic, abiotic @−0.9 V and biotic @−0.9 V, respectively.

reported surface roughness to affect the initial bacterial attachment and subsequent biofilm formation, with results[31,32] showing a negative correlation between bacterial adhesion and nano-roughness, while at micron-roughness, the correlation has generally been positive. In addition, some studies[33,34] have reported the different carbon contents in steel to affect the initial adhesion of bacteria, such that a higher carbon content results in a greater bacterial adhesion. In this study, the changes in carbon content were minimally affected by thermal treatment. After ruling out the possible factors, this suggests that the different HAZ

microstructures played a significant role in the initial bacterial attachment and subsequent corrosion.

To minimize the interference of the only possible factors in our study, we polished the HAZ microstructures with a 0.5 μm polishing paste and immersed them in the same experimental environment for 30, 60, and 90 min, consecutively. The distribution of the initial bacterial attachment on the different microstructures is shown in Fig. 11. The number of cells in each sample was counted in multiple areas, and the corresponding cell numbers are depicted in Fig. 12.
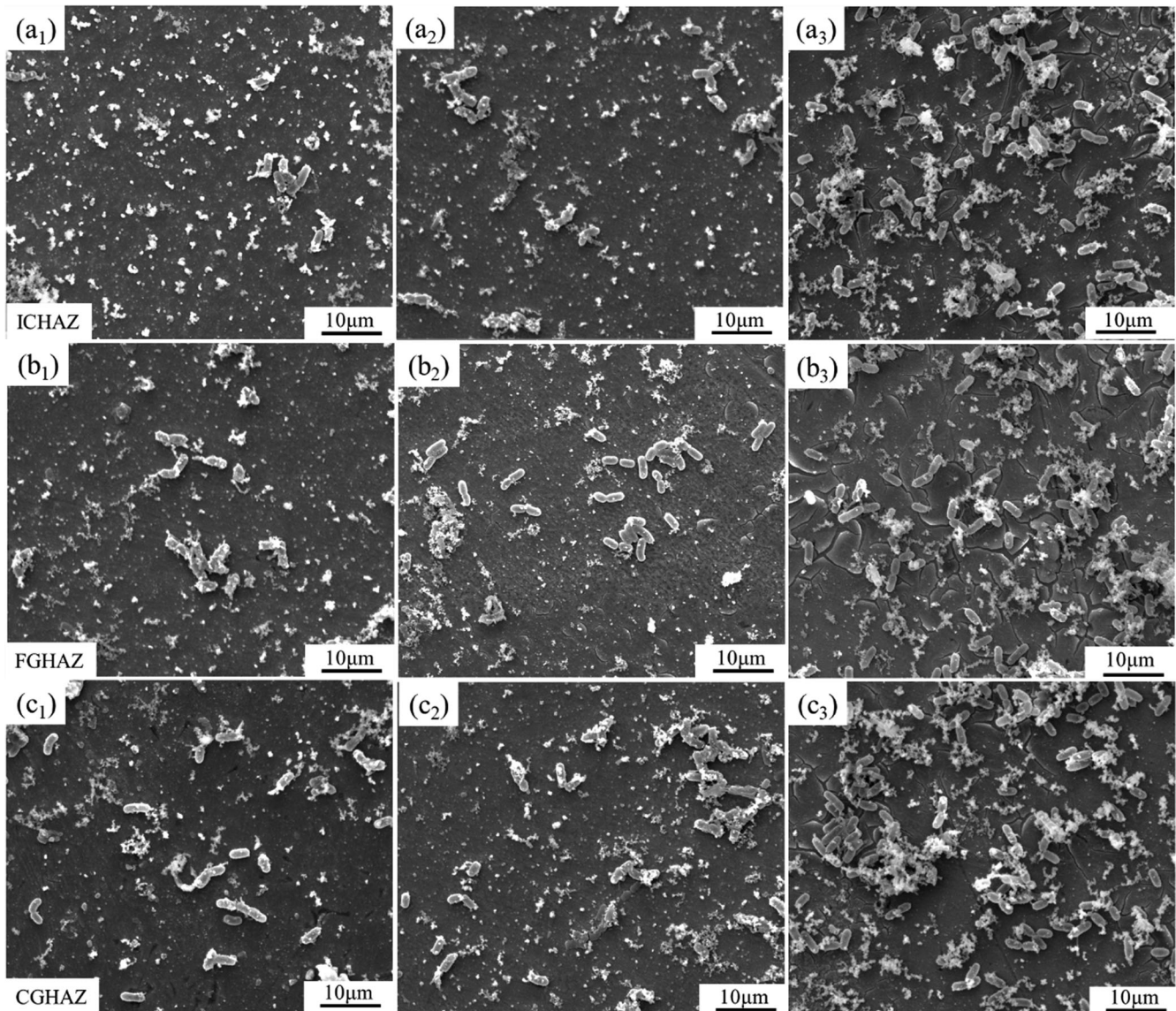
Fig. 11 Distribution of the initial bacterial attachment on HAZ. a ICHAZ. **b** FGHAZ. **c** CGHAZ. The subscripts 1–3 are 30 min, 60 min, and 90 min, respectively.

The bacteria are observed to be relatively uniformly distributed on the surface and gradually increase (in quantity) with increasing immersion time. When the immersion time reaches 90 min, the cells occupy almost the entire surface, indicating the number of bacterial cells on the different microstructures to be similar. Based on the statistical results of the cell numbers, we determined that the CGHAZ surface had the highest number of cells, followed by FGHAZ and IGHAZ (at different immersion times).

The grain size, dislocation density, and microstructure differences are all important factors that lead to corrosion differences in materials, and the thermodynamic stability of a material surface is closely related to the bacterial adhesion on it. It is believed that planktonic cells can recognize the surface by flagellar or pili movement and provide preferential selection for attachment[35,36]. To explore the relationship between the thermodynamic stability of the three different HAZ and bacterial adhesion, SKPFM was implemented to scan them, and the subsequent results are shown in Fig. 13. The coarse grain size of CGHAZ is accompanied by an increase in the prior austenite grain boundary, and a large granular bainite formation takes place inside the grains. Moreover, owing to the higher cooling temperature, the uniformity of the

grains decreases, the dislocations are trapped inside the grains, and the atoms are unevenly arranged in the large-angle grain boundaries, leading to a higher surface work function (Fig. 13c$_2$)[37]. These high thermodynamics provide a large number of active dissolution sites and electrons, facilitating for the bacteria to attach and obtain electrons[38]. ICHAZ and FGHAZ are composed of granular bainite and ferrite with small grains. As the cooling rate decreases, a large number of carbides precipitated, as shown by the white dots in Fig. 13a$_1$ and b$_1$, leading to a reduction in the carbon content, dislocation density, and local strain in the matrix, and subsequently, a decrease in the active dissolution position in the microstructure.

Relationship between stress and bacteria initial adhesion

The SSRT results confirmed that the *B. cereus*-inoculated medium increased the SCC susceptibility of the HAZ, especially for CGHAZ. Therefore, it is necessary to explore the effects of *B. cereus* on different microstructures under stressful conditions. The results of EBSD and quasi-in-situ initial adhesion SEM are shown in Fig. 14 and Supplementary Fig. 1. The inverse pole figure (IPF)

(Fig. 14a$_1$–c$_1$) shows CGHAZ to have the largest grain size, followed by FGHAZ and ICHAZ. The KAM mapping (Fig. 14a$_2$–c$_2$) reflects the density of the geometrically necessary dislocations, and the corresponding results suggest that the ICHAZ stress is evenly distributed, whereas the FGHAZ and IGHAZ stresses are obvious and concentrated. The subsequent 30 min immersion test topography (Fig. 14a$_3$–c$_3$) shows that *B. cereus* in different quantities can be detected on the surface of the sample, with some attached independently and some in clusters.
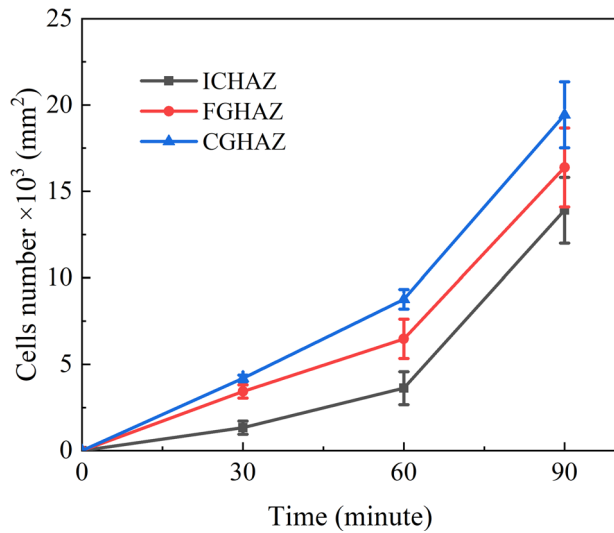

Fig. 12 Number of bacterial cells retained on HAZ. The number of bacteria attached to different microstructure surfaces of X80 steel in the same environment as the relationship of immersion time (error bars stand for the standard deviations from three independent samples).

To further elucidate the bacterial distribution behaviors under stress, the cells were manually marked in situ in the KAM phase mapping, and the corresponding results are shown in Fig. 15. The locally magnified maps clearly demonstrate the distribution of *B. cereus* in the low-stress, high-stress, or adjacent areas on different HAZ. Thus, we statistically analyzed the cell numbers and clusters in the whole marked region and normalized the *B. cereus* distribution. The corresponding results are listed in Table 1.

It is observed that 2.98% of the cells are distributed in the high stress region, 16–29% in the low stress region, and the remaining (i.e., more than half) occupy the adjacent transition region. These results show that the bacteria were preferentially distributed in the high/low-stress adjacent transition region. It is well known that the geometrically necessary dislocations in the high-stress regions are higher than those in the low-stress regions, increasing electrochemical activity. Thus, the initial adhesion selection of bacteria may be related to this property[39].

Based on the above analysis, the following conclusions can be drawn: (1) Compared with ICHAZ and FGHAZ, *B. cereus* had the most evident corrosion in CGHAZ. The CGHAZ surface allowed the adhesion of more bacteria in the early stages, which was ascribed to its higher surface thermodynamics. There were several dislocation-plugging and large-angle grain boundaries inside the microstructure, which provided active dissolution sites. (2) *B. cereus* increased the SCC sensitivity of different microstructures in the HAZ. The SCC of different microstructures in abiotic/biotic medium increased from 3.40–7.49% to 10.22–15.17% at OCP and from 22.81–26.51% to 35.76–39.60% at −0.9 V. Compared with ICHAZ and FGHAZ, *B. cereus* exhibited the greatest SCC sensitivity to CGHAZ. At −0.9 V, both ICHAZ and FGHAZ exhibited ductile fracture characteristics, while CGHAZ exhibited brittle fracture characteristics. (3) Different KAM values affected the initial bacterial adhesion. Compared to the high- and low-stress regions, 61–80% of *B. cereus* preferentially adhered to the high-/low-stress adjacent region.
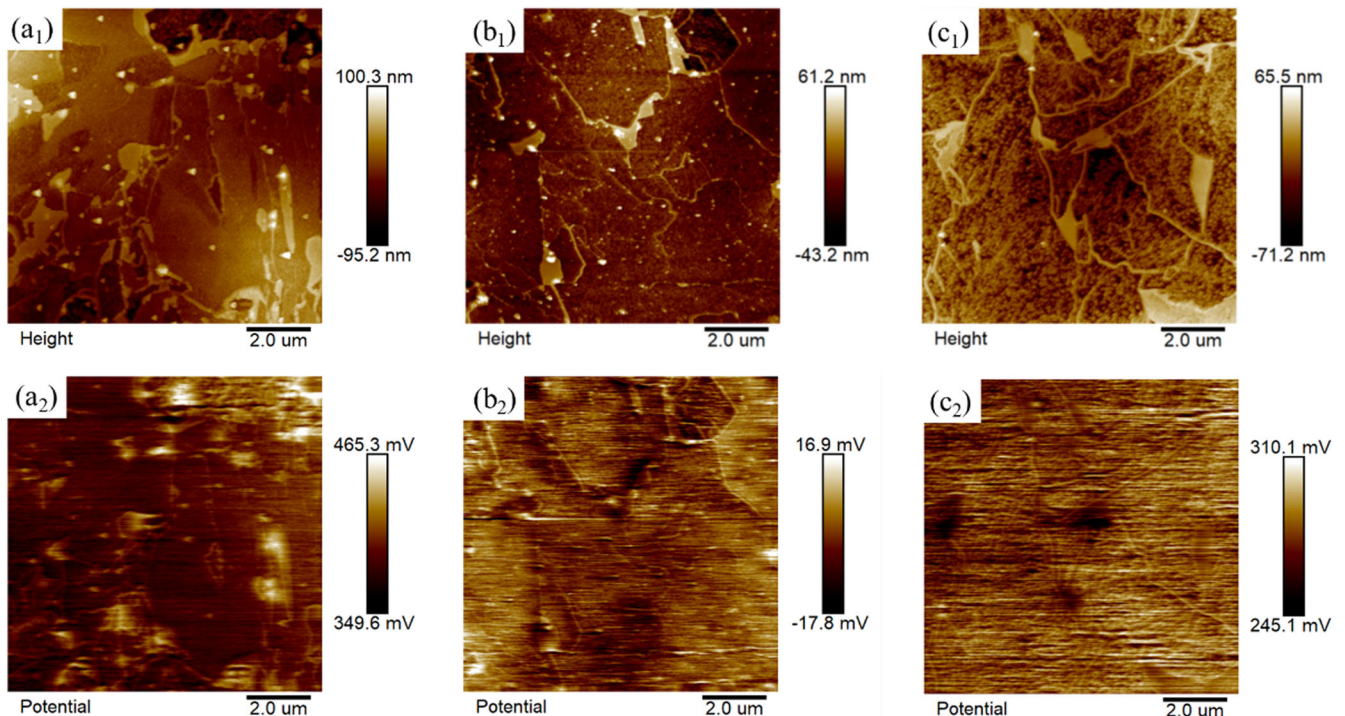

Fig. 13 SKPFM of different HAZ microstructures. a–c show ICHAZ, FGHAZ, and CGHAZ. **a$_1$–c$_1$** show topographic image. **a$_2$–c$_2$** show Volta potential map.
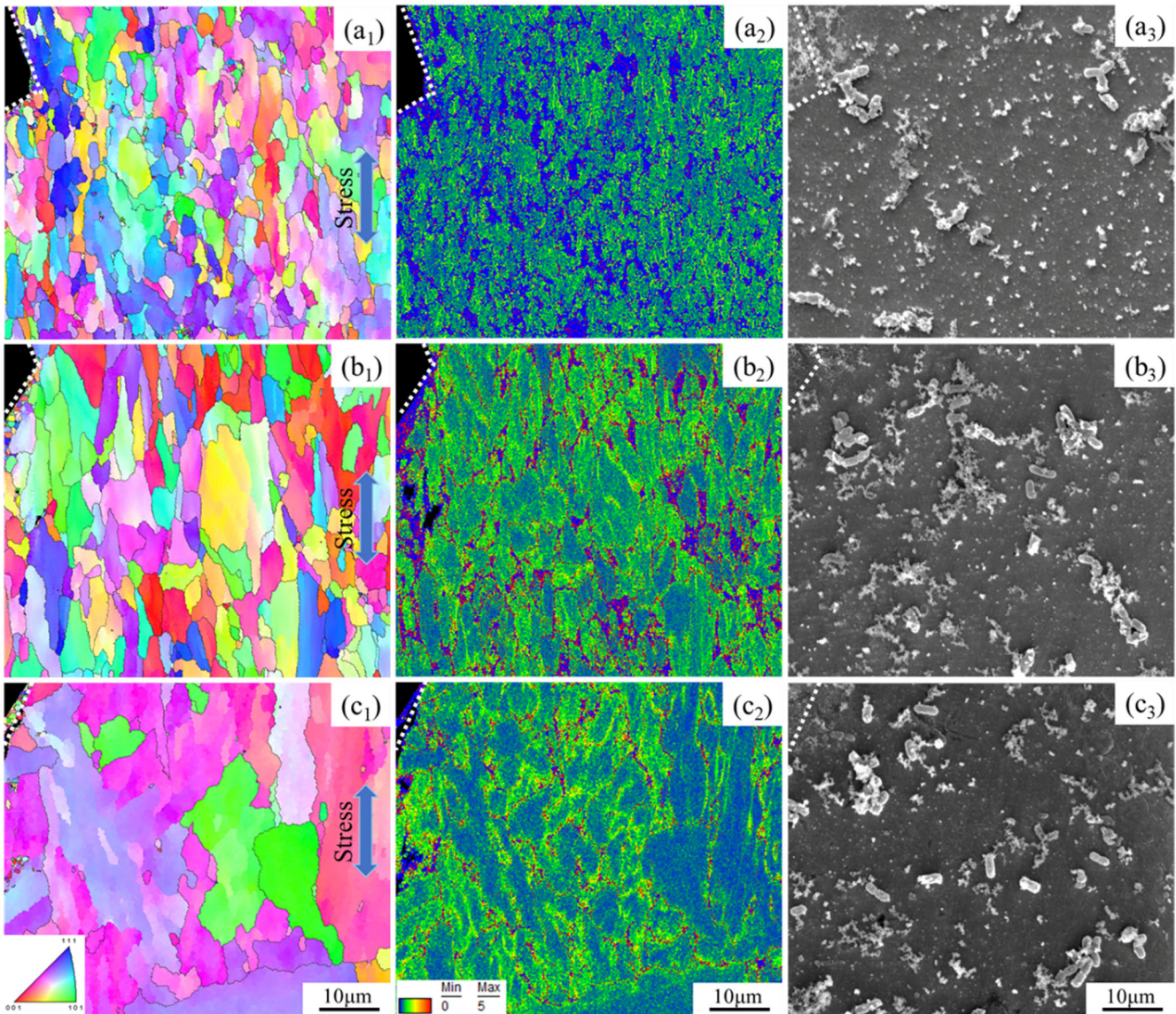
Fig. 14 EBSD analysis and in situ SEM morphology of the sample under 2% plastic strain. a–c show ICHAZ, FGHAZ, CGHAZ. The subscripts 1 are IPF. The subscripts 2 are KAM. The subscripts 3 are SEM.

METHODS

Material and HAZ microstructures

The material investigated in this study, X80 pipeline steel, was provided by Baoshan Iron & Steel Co. Ltd. The chemical composition of this pipeline steel was (wt%): 0.07 C, 0.24 Si, 2.16 Mn, 0.31 Cr, 0.35 Mo, 0.41 Ni, 0.25 Cu, 0.15 Nb, and Fe balance. The obtained microstructure was a typical granular bainite structure with a yield strength of 754 MPa. Typical HAZ microstructures were produced using a thermodynamic simulation tester (DIS; Gleeble 3500). The sample size was $80 \times 10 \times 10$ mm, and the energy of the test line was set to 17 kJ cm^{-1}. The preset and actual heating and cooling rates are shown in Fig. 16. After air cooling to room temperature, weld HAZ with different microstructures were formed.

By observing the microstructure, the characteristics of CGHAZ, FGHAZ, and ICHAZ were distinguished. Subsequently, the three microstructures were replicated via heat treatment. Andrews predicted the initial and complete austenitizing temperatures (A_{c1} and A_{c3}, respectively) for determining the appropriate peak temperatures of ICHAZ and FGHAZ microstructures, respectively,

and their corresponding empirical formulae were expressed as:

$$A_{c1}(°C) = 723 - 10.7\,\omega(Mn) - 13.9\,\omega(Ni) + 29\,\omega(Si) \\ + 16.9\,\omega(Cr) + 290\,\omega(As) + 6.38\,\omega(W) = 706°C,$$

$$A_{c3}(°C) = 910 - 203\omega(C)^{0.5} - 15.2\omega(Ni) + 44.7\omega(Si) \\ + 104\omega(V) + 32.5\omega(Mo) + 13.1\omega(W) = 871°C,$$

where ω denotes the mass fraction of each element. Several pieces of X80 steel were cut to dimensions of $20\,mm \times 10\,mm \times 3\,mm$ for the heat treatment. Combined with the T-C curve, for ICHAZ, FGHAZ, and CGHAZ, appropriate temperatures were selected at A_{C1}-A_{C3}, A_{C3}-1100 °C, and 1100–1320 °C, respectively. The cut X80 steel pieces were kept in a muffle furnace (HF-Kejing, KSL-1400X) at the corresponding temperature for 10 min and then cooled to room temperature. The pieces were then finely polished and etched with a 4% nital solution The subsequent microstructure was observed using a scanning electron microscope (SEM, XL30-FEG) until it was the same as that of the HAZ simulated by Gleeble. The peak
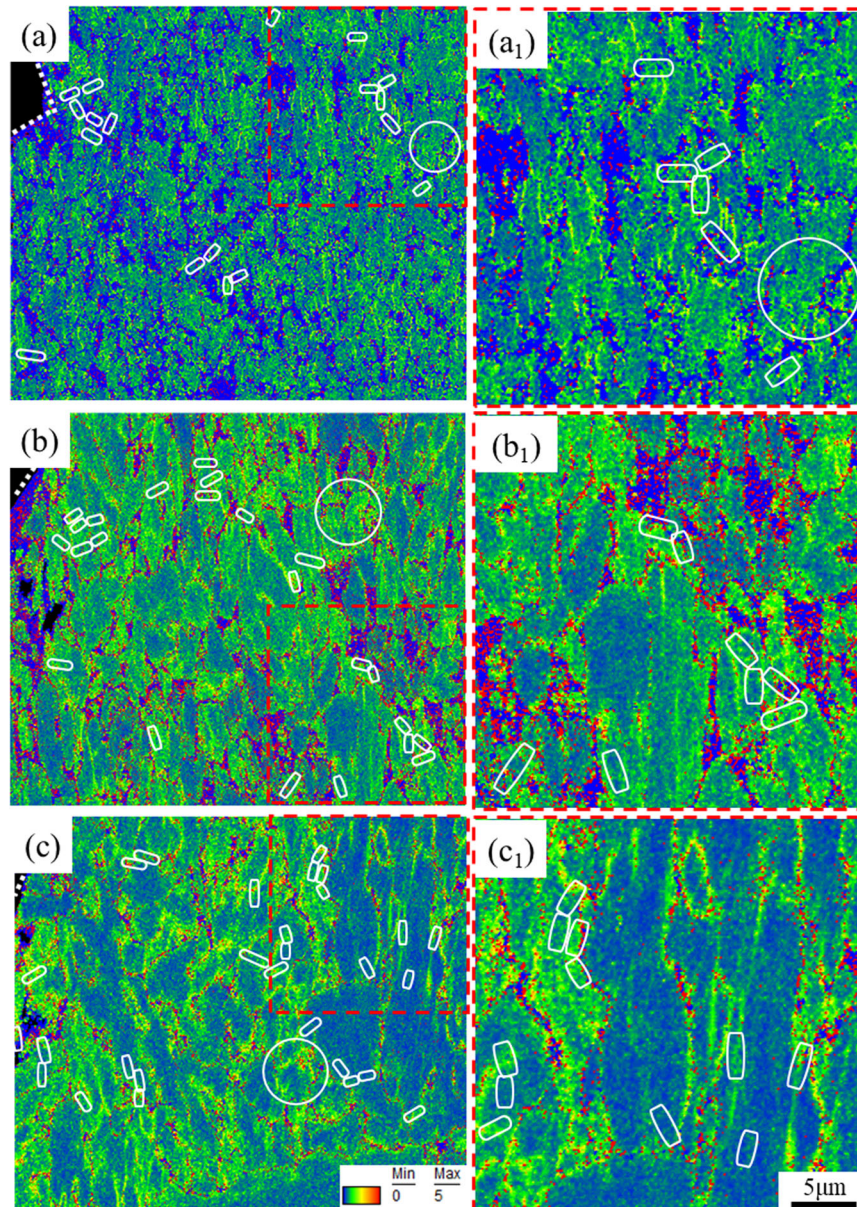
Fig. 15 KAM mapping with _B. cereus_. a–c show ICHAZ, FGHAZ, CGHAZ. The subscripts 1 correspond to locally magnified morphologies.

Table 1. Normalized statistical analysis results of the _B. cereus_ distribution behavior.

	Cells in high stress region	Cells in low stress region	Cells in adjacent transition region	Cluster number
ICHAZ	3	10	21	1
FGHAZ	2	9	45	2
CGHAZ	1	18	56	1
Proportion	2.9~8%	16~29%	61~80%	/

temperatures of ICHAZ, FGHAZ, and CGHAZ in this study were observed to be 750, 900, and 1300 °C, respectively.

All the specimens were progressively abraded with 150–2000 grit SiC papers, cleaned with deionized water and anhydrous ethanol, and finally dried in a cold air stream. All the samples were sterilized with glutaraldehyde and then exposed to UV light for at least 30 min prior to the test to ensure that they were not contaminated.

Bacteria and culture medium

B. cereus, a typical NRB, was isolated from the surrounding soil of an X80 pipeline steel specimen (100 mm × 75 mm × 5 mm) that had been buried for two years in Beijing soil (NL 39°79, EL 116°35, average temperature 12.9°C, moisture 14.38, salinity 0.198%, pH 6.96). Evolutionary trees and their nitrate reducibility were analyzed as described in our previous study[40]. The composition of the near-neutral pH solution was (g·L^{-1}): 0.5 yeast extract,

1 tryptone, 1 NaCl, 1 NaNO₃, 0.483 NaHCO₃, 0.122 KCl, 0.137 CaCl₂, and 0.131 MgSO₄·7H₂O. Before the experiment, the medium was sterilized at 121 °C for 20 min, and cooled under a continuous stream of 5% CO_2 balanced with N_2 for 2 h to achieve an anaerobic and near-neutral pH condition.

For the biotic medium, bacterial seeds were cultured in the above solution at 30 °C for 24 h at a ratio of 1:100 (v/v). For the abiotic medium, the culture medium was not inoculated with any bacteria, ensuring that the whole experimental process was uncontaminated. All the experiments were sealed and performed at 30 °C without oxygen, unless otherwise specified.

Electrochemical test
HAZ specimens with dimensions of 10 mm × 10 mm × 2 mm were connected to a copper wire and sealed with epoxy resin, leaving 1 cm² as the working electrode (WE). A platinum sheet and saturated calomel electrode (SCE) were used as the counter and reference electrodes, respectively.
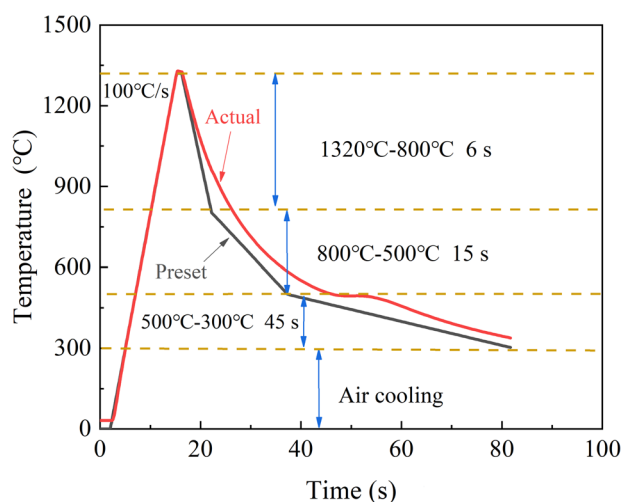

Fig. 16 Gleeble 3500 simulates the HAZ process. Preset and actual temperature changes with experiment time.

The electrochemical tests were performed through a workstation (Gamry, Reference 600+) using a typical three-electrode system. After inoculation, electrochemical impedance spectroscopy (EIS) was performed for 1, 3, 7, and 14 d at a sinusoidal voltage signal of 10 mV in the frequency range of 10^{-2}–10^4 Hz. Fast and slow sweep potential polarization curves were determined for the specimens after they were immersed in the inoculation medium for 3 d. The scanning range of the polarization curves was from −1.3 to 0 V (vs. Ref), while the scanning rates for the fast and slow potential curves were 0.5 and 50 mV s⁻¹, respectively. The EIS data and polarization curves were analyzed using the Zsimpwin software (Scribner) and Echem Analyst (Gamry), respectively.

Morphology analysis
After completing the 14-day EIS, the samples were carefully removed and immersed in a 2.5% glutaraldehyde solution for 8 h at 4 °C in a refrigerator. The specimens were then dehydrated with ethanol (50%, 60%, 70%, 80%, 90%, and 100% (v/v) consecutively) for 8 min, followed by drying naturally. The morphology was observed via SEM with a beam voltage of 25 kV. The corrosion product elements and their structures were analyzed via energy-dispersive X-ray spectroscopy (EDX). After observation, the samples were cleaned in acetone followed by immersion in a derusting solution (3.5 g hexamethylenetetramine was added to 500 mL hydrochloric acid and 500 mL deionized water) to remove any corrosion products. Next, the morphology of the corrosion pits was observed via confocal laser scanning microscopy (CLSM, Keyence VK-X250).

Slow strain rate tensile
Tensile specimens and experimental devices were used in the experiment, as shown in Fig. 17 a and b, respectively. After polishing and UV irradiation, the tensile specimen were sealed with silica gel, installed in a sealed box containing CE and RE, and subjected to UV irradiation for at least 30 min. The solution inoculated with *B. cereus* was injected into the device and kept at OCP or −0.9 V for 3 d. The solution cell with the tensile samples was then fixed on a tensile testing machine (Letry, WDML-30 kN). A pre-force of 1000 N was added to eliminate the crevice inside the machine and fixture gap. The strain rate was set to
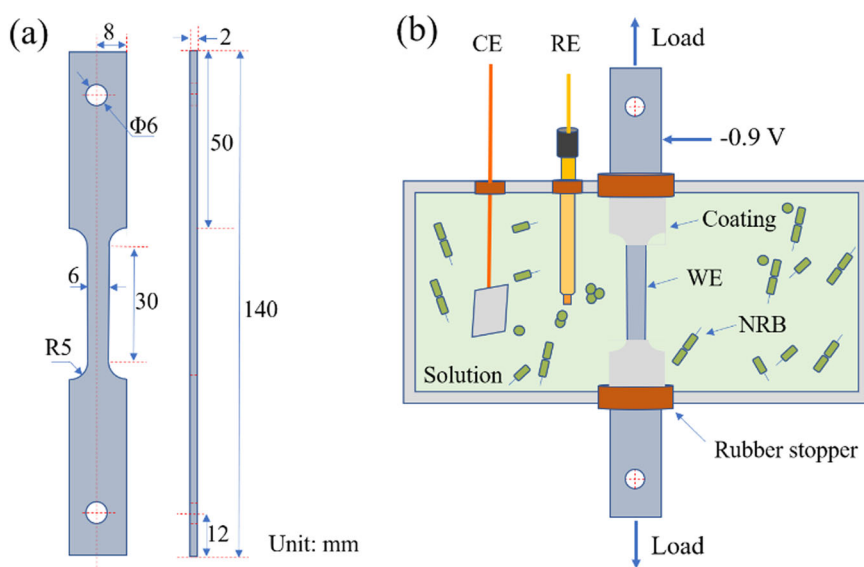

Fig. 17 Schematic diagram of the SSRT samples and solution cell. a is detailed size of sample, **b** is schematic diagram of the solution cell for SSRT.

$1 \times 10^{-6}\,s^{-1}$, the same order of magnitude as that of a typical SCC crack propagation rate.

Previous studies[27] have shown the *B. cereus* system to have the maximum effect on the SCC sensitivity of X80 steel at $-0.9\,V$. attributed to the potential having an effect on both the hydrogen embrittlement and physiological activities of *B. cereus*. Therefore, the same test parameters were used to investigate the effects of *B. cereus* on HAZ.

After the SSRT test, the decrease in the reduction in area (I_ψ) was calculated using the following equation to evaluate the fracture susceptibility of X80 steel.

$$I_\psi = \left(1 - \frac{\psi_s}{\psi_0}\right) \times 100\%, \tag{1}$$

where ψ_s and ψ_0 are the percentage reductions in area in the test environment and air, respectively. The fracture specimens were cut to remove the excess part, corrosion products were cleaned as described in morphology analysis, and fracture and lateral surfaces of the specimens were observed via SEM.

Microscopic surface analysis

The samples for electron backscatter diffraction (EBSD) and scanning Kelvin probe force microscopy (SKPFM) were prepared as follows: three different HAZ tensile specimens were subjected to SSRT testing at 2% plastic strain. The most central 10 mm length was then cut to 10 mm × 6 mm × 2 mm specimens. After a series of mechanical polishing, electrolytic etching, and position marking procedures, the EBSD and SKPFM samples were prepared. The subsequent EBSD data was acquired using TSL data acquisition software integrated with JSM-6301. Kernel average misorientation (KAM) mapping was performed using the 1st nearest neighbor method. SKPFM tests were performed using an atomic force microscope (Bruker, Multimode VIII) in ScanAsyst-air mode to obtain the topologies and Volta potentials of the surface, which were analyzed using the NanoScope Analysis software.

REFERENCES

1. Qiao, Q. et al. Failure analysis of corrosion at an inhomogeneous welded joint in a natural gas gathering pipeline considering the combined action of multiple factors. *Eng. Failure Anal.* **64**, 126–143 (2016).
2. Shirinzadeh, M., Mohammadi, J., Behnamian, Y., Eghlimi, A. & Mostafaei, A. Metallurgical investigations and corrosion behavior of failed weld joint in AISI 1518 low carbon steel pipeline. *Eng. Failure Anal.* **53**, 78–96 (2015).
3. Sahraoui, Y., Benamira, M., Nahal, M., Nouadria, F. & Chateauneuf, A. The effect of welded joint repair on a corroded pipeline reliability subjected to the hardness spatial variability and soil aggressiveness. *Eng. Failure Anal.* **118**, 104854 (2020).
4. Mohammadi, F., Eliyan, F. F. & Alfantazi, A. Corrosion of simulated weld HAZ of API X-80 pipeline steel. *Corros. Sci.* **63**, 323–333 (2012).
5. Li, Y. et al. Effect of cathodic potential on stress corrosion cracking behavior of different heat-affected zone microstructures of E690 steel in artificial seawater. *J. Mater. Sci. Technol.* **64**, 141–152 (2021).
6. Wang, L. W. et al. In situ corrosion characterization of simulated weld heat affected zone on API X80 pipeline steel. *Corros. Sci.* **85**, 401–410 (2014).
7. Ma, H. C. et al. Comparative study on corrosion fatigue behaviour of high strength low alloy steel and simulated HAZ microstructures in a simulated marine atmosphere. *Int. J. Fatigue* **137**, 105666 (2020).
8. Wu, W., Liu, Z. Y., Li, X. G., Du, C. & Cui, Z. Influence of different heat-affected zone microstructures on the stress corrosion behavior and mechanism of high-strength low-alloy steel in a sulfurated marine atmosphere. *Mater. Sci. Eng. A* **759**, 124–141 (2019).
9. Zhu, J. Y. et al. Galvanic corrosion of a welded joint in 3Cr low alloy pipeline steel. *Corros. Sci.* **111**, 391–403 (2016).
10. Dao, V. H., Ryu, H. K. & Yoon, K. B. Leak failure at the TP316L welds of a water pipe caused by microbiologically influenced corrosion. *Eng. Failure Anal.* **122**, 105244 (2021).
11. Ress, J. et al. Microbiologically influenced corrosion of welded AISI 304 stainless steel pipe in well water. *Eng. Failure Anal.* **116**, 104734 (2020).
12. Devendranath, R. K. et al. Microstructure, mechanical properties and biocorrosion behavior of dissimilar welds of AISI 904L and UNS S32750. *J. Manuf. Process* **30**, 27–40 (2017).
13. Arun, D., Vimala, R. & Devendranath Ramkumar, K. Investigating the microbial-influenced corrosion of UNS S32750 stainless-steel base alloy and weld seams by biofilm-forming marine bacterium Macrococcus equipercicus. *Bioelectrochemistry* **135**, 107546 (2020).
14. Antony, P. J., Singh Raman, R. K., Kumar, P. & Raman, R. Corrosion of 2205 duplex stainless steel weldment in chloride medium containing sulfate-reducing bacteria. *Metall. Mater. Trans. A* **39**, 2689–2697 (2008).
15. Liduino, V. S., Lutterbach, M. T. S. & Sérvulo, E. F. C. Biofilm activity on corrosion of API 5L X65 steel weld bead. *Colloids Surf. B. Biointerfaces* **172**, 43–50 (2018).
16. Stipaničev, M., Rosas, O., Basseguy, R. & Turcu, F. Electrochemical and fractographic analysis of microbiologically assisted stress corrosion cracking of carbon steel. *Corros. Sci.* **80**, 60–70 (2014).
17. Wei, B. X. et al. Effect of uniaxial elastic stress on corrosion of X80 pipeline steel in an acidic soil solution containing sulfate-reducing bacteria trapped under disbonded coating. *Corros. Sci.* **193**, 109893 (2021).
18. Guo, L. et al. Multidimensional insights into the corrosion inhibition of 3,3-dithiodipropionic acid on Q235 steel in H_2SO_4 medium: a combined experimental and in silico investigation. *J. Colloid Interface Sci* **570**, 116–124 (2020).
19. Javaherdashti, R., Raman, R., Panter, C. & Pereloma, E. Microbiologically assisted stress corrosion cracking of carbon steel in mixed and pure cultures of sulfate reducing bacteria. *Int. Biodeterior. Biodegrad.* **58**, 27–35 (2006).
20. Lv, M., Chen, X., Li, Z. & Du, M. Effect of sulfate-reducing bacteria on hydrogen permeation and stress corrosion cracking behavior of 980 high-strength steel in seawater. *J. Mater. Sci. Technol.* **92**, 109–119 (2021).
21. Sun, D. X., Wu, M. & Xie, F. Effect of sulfate-reducing bacteria and cathodic potential on stress corrosion cracking of X70 steel in sea-mud simulated solution. *Mater. Sci. Eng. A* **721**, 135–144 (2018).
22. Liu, B., Li, Z. Y., Yang, X. J., Du, C. & Li, X. Microbiologically influenced corrosion of X80 pipeline steel by nitrate reducing bacteria in artificial Beijing soil. *Bioelectrochemistry* **135**, 107551 (2020).
23. Mulla, A. et al. Diversity of culturable nitrate-reducing bacteria from the Arabian Sea oxygen minimum zone. *Deep Sea Res. Part II Top. Stud. Oceanogr* **156**, 27–33 (2018).
24. Huang, Y. et al. Responses of soil microbiome to steel corrosion. *npj Biofilms Microbiomes* **7**, 6 (2021).
25. Al-Nabulsi, K. M., Al-Abbas, F. M., Rizk, T. Y. & Salameh, A. a. E. M. Microbiologically assisted stress corrosion cracking in the presence of nitrate reducing bacteria. *Eng. Failure Anal.* **58**, 165–172 (2015).
26. Liu, B. et al. Corrosion mechanism of nitrate reducing bacteria on X80 steel correlated to its intermediate metabolite nitrite. *Constr. Build. Mater.* **303**, 124454 (2021).
27. Liu, B., Liu, M. H., Liu, Z. Y., Du, C. & Li, X. Nitrate-reducing-bacteria-assisted hydrogen embrittlement of X80 steel in a near-neutral pH solution. *Corros. Sci.* **202**, 110317 (2022).
28. Song, L., Liu, Z., li, X. & Du, C. Stress corrosion cracking of simulated weld heat-affected zone on X100 pipeline steel in carbonate/bicarbonate solution. *J. Mater. Eng. Perform.* **29**, 2574–2585 (2020).
29. Liu, Z. Y., Li, X. G. & Cheng, Y. F. Mechanistic aspect of near-neutral pH stress corrosion cracking of pipelines under cathodic polarization. *Corros. Sci.* **55**, 54–60 (2012).
30. Liu, Z., li, X., Du, C. & Cheng, Y. Local additional potential model for effect of strain rate on SCC of pipeline steel in an acidic soil solution. *Corros. Sci.* **51**, 2863–2871 (2009).
31. Yang, K. et al. Bacterial anti-adhesion surface design: surface patterning, roughness and wettability: a review. *J. Mater. Sci. Technol.* **99**, 82–100 (2022).
32. Chinnaraj, S. B. et al. Modelling the combined effect of surface roughness and topography on bacterial attachment. *J. Mater. Sci. Technol.* **81**, 151–161 (2021).
33. Javed, M. A., Neil, W. C., Stoddart, P. & Wade, S. Influence of carbon steel grade on the initial attachment of bacteria and microbiologically influenced corrosion. *Biofouling* **32**, 109–122 (2016).
34. Xu, D. K. & Gu, T. Y. Carbon source starvation triggered more aggressive corrosion against carbon steel by the Desulfovibrio vulgaris biofilm. *Int. Biodeterior. Biodegrad.* **91**, 74–81 (2014).

35. Uneputty, A. et al. Strategies applied to modify structured and smooth surfaces: a step closer to reduce bacterial adhesion and biofilm formation. *Colloids Interface Sci. Commun.* **46**, 100560 (2022).

36. Kreve, S. & Reis, A. C. D. Bacterial adhesion to biomaterials: what regulates this attachment? *Jpn. Dent. Sci. Rev.* **57**, 85–96 (2021).

37. Moteshakker, A. & Danaee, I. Microstructure and corrosion resistance of dissimilar weld-joints between duplex stainless steel 2205 and austenitic stainless steel 316L. *J. Mater. Sci. Technol.* **32**, 282–290 (2016).

38. Daughney, C. J., Fein, J. B. & Yee, N. A comparison of the thermodynamics of metal adsorption onto two common bacteria. *Chem. Geol.* **144**, 161–176 (1998).

39. Yang, X. J. et al. Stress-assisted microbiologically influenced corrosion mechanism of 2205 duplex stainless steel caused by sulfate-reducing bacteria. *Corros. Sci.* **173**, 108746 (2020).

40. Liu, B., Sun, M. H., Lu, F. Y., Du, C. & Li, X. Study of biofilm-influenced corrosion on X80 pipeline steel by a nitrate-reducing bacterium, *Bacillus cereus*, in artificial Beijing soil. *Colloids Surf. B. Biointerfaces* **197**, 111356 (2021).

ACKNOWLEDGEMENTS

AUTHOR CONTRIBUTIONS

B.L.: Conceptualization, methodology, investigation, and writing. J.Y.: Conceptualization, methodology, and investigation. C.D.: Project administration and conceptualization. Z.L.: Review and editing. W.W.: Formal analysis. Supervision. X.L.: Resources.

COMPETING INTERESTS

The authors declare no competing interests.

ADDITIONAL INFORMATION

Supplementary information The online version contains supplementary material available at https://doi.org/10.1038/s41529-023-00333-w.

Correspondence and requests for materials should be addressed to Cuiwei Du or Zhiyong Liu.

Reprints and permission information is available at http://www.nature.com/reprints

Publisher's note Springer Nature remains neutral with regard to jurisdictional claims in published maps and institutional affiliations.